Steady-state and transient photoconductivity in *c*-axis GaN nanowires grown by nitrogen-plasma-assisted molecular beam epitaxy

N. A. Sanford,[1,a)] P. T. Blanchard,[1] K. A. Bertness,[1] L. Mansfield,[1] J. B. Schlager,[1] A. W. Sanders,[1] A. Roshko,[1] B. B. Burton,[2] and S. M. George[2]
[1]*Optoelectronics Division 815, National Institute of Standards and Technology, Boulder, Colorado 80305, USA*
[2]*Department of Chemistry and Biochemistry, University of Colorado, Boulder, Colorado 80309, USA*

(Received 23 February 2009; accepted 22 November 2009; published online 12 February 2010)

Analysis of steady-state and transient photoconductivity measurements at room temperature performed on *c*-axis oriented GaN nanowires yielded estimates of free carrier concentration, drift mobility, surface band bending, and surface capture coefficient for electrons. Samples grown (unintentionally *n*-type) by nitrogen-plasma-assisted molecular beam epitaxy primarily from two separate growth runs were examined. The results revealed carrier concentration in the range of $(3-6)\times10^{16}$ cm^{-3} for one growth run, roughly $5\times10^{14}-1\times10^{15}$ cm^{-3} for the second, and drift mobility in the range of 500–700 $cm^2/(V\ s)$ for both. Nanowires were dispersed onto insulating substrates and contacted forming single-wire, two-terminal structures with typical electrode gaps of $\approx3-5$ μm. When biased at 1 V bias and illuminated at 360 nm (3.6 mW/cm^2) the thinner (≈100 nm diameter) nanowires with the higher background doping showed an abrupt increase in photocurrent from 5 pA (noise level) to 0.1–1 μA. Under the same conditions, thicker (151–320 nm) nanowires showed roughly ten times more photocurrent, with dark currents ranging from 2 nA to 1 μA. With the light blocked, the dark current was restored in a few minutes for the thinner samples and an hour or more for the thicker ones. The samples with lower carrier concentration showed similar trends. Excitation in the 360–550 nm range produced substantially weaker photocurrent with comparable decay rates. Nanowire photoconductivity arises from a reduction in the depletion layer via photogenerated holes drifting to the surface and compensating ionized surface acceptors. Simulations yielded (dark) surface band bending in the vicinity of 0.2–0.3 V and capture coefficient in the range of $10^{-23}-10^{-19}$ cm^2. Atomic layer deposition (ALD) was used to conformally deposit ≈10 nm of Al_2O_3 on several devices. Photoconductivity, persistent photoconductivity, and subgap photoconductivity of the coated nanowires were increased in all cases. TaN ALD coatings showed a reduced effect compared to the Al_2O_3 coated samples.
 [doi:10.1063/1.3275888]

I. INTRODUCTION

Wide-bandgap III-nitride nanowires (NWs) are gaining increased attention for applications involving nanophotonics and nanoelectronics.[1–3] GaN NW structures may be grown by a variety of methods that are now briefly summarized. Laser catalyzed growth has been used to grow $[11\bar{2}0]$ (*a*-axis) oriented NWs.[1] Core-shell GaN NW heterostructure light-emitting diodes (LEDs) have been realized where catalyst grown *a*-axis cores were subsequently overgrown with InGaN/AlGaN shells.[2] However, extensive transmission electron microscopy (TEM) analysis on *a*-axis GaN NWs reveals that they can suffer from a high density of extended defects and basal plane stacking faults.[4] By contrast, [0001] (*c*-axis) oriented GaN NWs grown by nitrogen-plasma-assisted molecular beam epitaxy (PAMBE) have been shown to be essentially free of strain and defects when examined by x-ray diffraction, TEM, photoluminescence (PL), and nanomechanical studies.[5–9] The characteristically low strain and low defect density of these PAMBE grown *c*-axis NWs have been observed earlier by other workers (Ref. 10 and references therein), and dense arrays of such structures are being used to realize a new class of GaN LED devices.[11,12]

An important feature of GaN NWs, given a particular doping level and surface band bending, is that they can be nearly or fully depleted of charge carriers and may conduct in a space-charge limited fashion in certain circumstances.[13] Indeed, it is the control of the depletion layer thickness that enables field effect transistor (FET) sensors based on these structures to function via electrostatic gating by surface adsorbates.[14,15] Control of the depletion layer thickness is also important for the operation of these NW devices as photoconductive optical detectors as will become evident within the context of this paper. Back-gated NW FET devices are commonly used to estimate transport properties of the NWs themselves (e.g., carrier concentration and mobility).[3] However, in our experience such approaches for estimating the transport properties of NWs can be unreliable since we find these devices often display gate hysteresis and drift.[16] It is thus desirable to establish alternative approaches for estimating transport properties in NW structures; in this regard, photoconductivity (PC) can offer new insights.

[a)]Electronic mail: sanford@boulder.nist.gov.

PC studies of GaN NWs have been reported by a number of authors. Calarco *et al.*[13] described dark conductivity and PC studies as a function of NW diameter for *c*-axis oriented unintentionally doped (UID) *n*-type NWs grown by PAMBE. They concluded that the surface band bending (in the dark) was approximately 0.55 V for samples thick enough to be undepleted. They showed that the PC mechanism arose from photoexcited holes drifting to the NW surface, screening the depletion field, thereby increasing the diameter of the neutral region and increasing the NW conductivity. It is interesting to note that the basic mechanism of photoexcited holes screening a depletion field to promote gain in planar III-nitride photoconductive detectors has been discussed earlier.[17]

PC studies of deep levels in metal-organic chemical-vapor deposition (MOCVD) Ni-catalyst grown UID *a*-axis GaN NWs were performed by Armstrong *et al.*[18] where it was argued that majority carrier photoemission from deep levels within the depletion region resulted in increased NW conductivity. PC studies of Si-doped *n*-type PAMBE grown *c*-axis NWs were reported by Richter *et al.*[19] where they observed that Si incorporation would change the NW growth morphology from essentially uniform in thickness to tapered and conical. They noted that fitting dark current data on a variety of NWs should in principle permit determination of carrier mobility. Mansfield *et al.*[20] also reported dark conductivity and PC studies in PAMBE grown Si-doped *c*-axis GaN NWs, compared the results with back-gated FET behavior on the same samples, and numerical simulations of FET behavior. Moreover, Mansfield *et al.* estimated the uncertainty involved when attempting to reconcile free carrier concentration, drift mobility, and band bending using dark current and PC data, and also showed that the incorporation of Si in the PAMBE growth process did not appear to substantially alter the NW growth morphology, in contrast to the preceding reference.

II. EXPERIMENTAL PROCEDURE AND DATA ANALYSIS

A number of parameters and conventions appearing in this paper are defined as follows: the background *n*-type donor density is N_d and it is assumed that such donors are fully ionized, n_L is the integrated free charge per unit length along a NW, n_{ph} is the density of photogenerated holes, D_i is the diameter of a cylinder that inscribes a NW of hexagonal cross section with $R_i=D_i/2$, D_c and R_c are the same respective parameters for a circumscribing cylinder, D_m is the diameter of a hypothetical NW of circular cross section with $R_m=D_m/2$, R_e^f is the radius of a cylinder with an equivalent cross sectional area as a hexagon defined by the circumscribing cylinder with radius R_c, the power intensity illuminating a sample at a wavelength λ (in nanometers) is $P(\lambda)$, the total steady-state current (dark current and photocurrent) under constant illumination is I_p, the initial transient photocurrent at the instant illumination ceases is I_p^o, the decaying current that persists after illumination ceases is $I_p(t)$, the maximum "flatband" current conducted in a NW with zero depletion layer thickness is I_f, and the dark current that remains after persistent photoconductivity (PPC) has relaxed is I_d. Other parameters are defined where they appear.

This portion of the paper is organized as follows: Section II A describes NW sample growth and fabrication. Section II B presents an experimental study of steady-state dark current and photocurrent and focuses on samples from growth run B738. Section II C presents a cylindrical depletion model which is applied to samples displaying nonzero dark current. Section II D presents a model describing the time decay of persistent PC. Section II E illustrates the effect on PC that result when NWs are coated with atomic layer deposition (ALD) films. Subbandgap PC is also described in this section.

A. NW growth and processing to fabricate two-terminal photoconductive test structures

The *c*-axis oriented GaN NWs used in this study were grown by PAMBE on Si(111) substrates. Details on the growth, spectroscopic studies, and mechanical properties of NWs grown in our laboratory are given elsewhere.[5–9] Notable in these background studies is that the PAMBE grown wires are essentially free of strain and defects. Indeed, TEM reveals that basal plane stacking faults are *only* found in the interfacial region where the NWs nucleate on the Si substrate and are not found elsewhere in the NWs. Depending on the precise growth conditions, D_c for the wires examined ranged from roughly 100 to 700 nm. The NWs produced in a particular growth run were generally well formed elongated hexagonal cylinders that were roughly uniform in diameter. The growth rate was in the range from 100 to 300 nm/h and NWs were grown to lengths ranging from 5 to 20 μm.

NWs were ultrasonically stripped off of the Si(111) growth substrates in an isopropanol bath and dispersed with a micropipette onto fused quartz substrates and oxidized Si substrates. Photoconductive test structures were fabricated in two separate formats: (i) wires lying flat on the dispersal substrates and electrically contacted at their ends and (ii) wires electrically contacted at their ends but suspended horizontally above the substrates by a few hundred nanometers, thus forming NW bridge structures. Examples of contacted NWs dispersed flat, and forming a bridge structure, are shown in Figs. 1(a) and 1(b), respectively. The NWs are quite flexible and, as illustrated in Fig. 1(c), in certain instances, a bridging wire would bend down into contact with the substrate without breaking or losing electrical continuity. Various test structures fabricated from NWs taken from the separate PAMBE growth runs are summarized in Table I. For NWs of comparable D_c taken from a common growth run, there was no significant difference in photoconductive behavior for test structures composed of wires lying flat on dispersal substrates or in the form of bridge structures. The fabrication scheme for NW electrical contacts is now described.

Contacts were formed by electron beam deposition of 20 nm of Ti followed by 200 nm of Al. Subsequent lift-off photolithography yielded a dense array of indexed electrodes with single NWs occasionally bridging an electrode pair. The samples were then processed by rapid thermal annealing

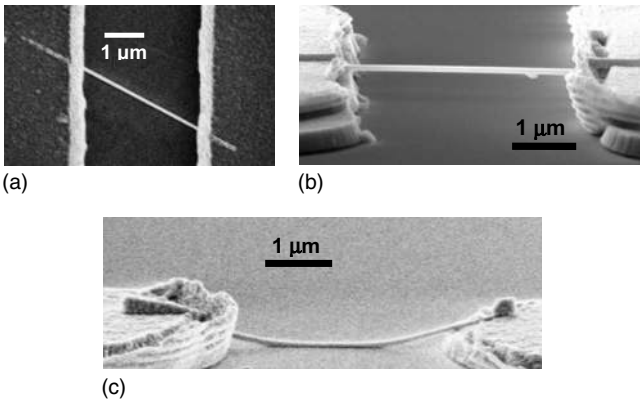

FIG. 1. (a) Single NW lying flat on a fused quartz substrate and electrically contacted at the two ends. This image corresponds to sample 7, as enumerated in Table I. (b) Example of a NW bridge structure. The sample rests roughly 200 nm above the surface of the fused quartz substrate. (c) NW flexibility is illustrated in this image. During dielectrophoresis alignment, the portion of the NW between the pads sagged and adhered to the substrate via van der Waals forces. Despite appearance to the contrary, this device was unbroken and exhibited electrical continuity.

(RTA) in a flowing atmosphere [1.4 SLM (SLM denotes standard liters/minute)] of 5% H_2/95% Ar. The RTA temperature schedule was ramp from ambient to 100 °C in 5 min, dwell at 100 °C for 5 min, ramp to 500 °C in 10 s, dwell at 500 °C for 60 s, and cool to ambient. The assembly of NW bridge structures employed methods of ac dielectrophoresis[21] to orient the NWs between Ti electrode pads that were photolithographically defined on the substrates. In these experiments, NWs in a solvent suspension were dispersed onto the substrate while an ac voltage was applied between the electrode pads. As the solvent evaporated, the wires would come to rest suspended between adjacent electrode pads, thus forming bridges with the wires elevated a few hundred nanometers above the substrate. Contacts to ends of these bridging NWs were subsequently made using another lithography step and the same Ti/Al metallization and RTA procedure described previously. The electrical conductivity enabled by our metallization and annealing scheme is expected to arise from the diffusion of N from the NW into the Ti layer, thereby producing a TiN layer with a reduced work function compared to the pure metal. Additionally, the N-depleted region in the GaN under the metal contact is expected to have enhanced *n*-type conductivity via the formation of N vacancies.[22] With this processing scheme, a conservative estimate[22–24] of the resulting specific contact resistivity is in the range of $(1-10)\times10^{-5}$ Ω cm^2. Anticipating the discussion that follows below, we estimated that N_d is approximately $(3-6)\times10^{16}$ cm^{-3} for growth batch B738 and approximately $5\times10^{14}-1\times10^{15}$ cm^{-3} for batch B992. Following Mohney *et al.*[25] and assuming an estimated range for drift mobility μ of 500–700 cm^2/(V s), we find that the contact resistance is typically ten times less than the NW resistance considering the typical ranges of NW diameters and electrode gaps given in Table I.

We note that our estimate for μ is consistent with the best report (that we are aware of) for MBE grown GaN films. Nikishin *et al.*[26] reported a Hall mobility of 800 ± 100 cm^2/(V s) for crack-free molecular beam epitaxy (MBE) grown GaN with a *n*-type background of $(2-3)\times10^{16}$ cm^3. Using a conservative estimate for the Hall factor of roughly 1.2–1.3 for GaN,[27] our presumed range in drift mobility μ is reasonable and is also consistent with the estimated results that follow below. Taken together, these observations and estimates lead us to conclude that most of the voltage is dropped across the NW, and the resistance of the contacts may be ignored in the subsequent analysis.

TABLE I. Summary of samples used in the present study. All relevant parameters are defined in the text, with the exception that the "A" and T" designations refer to ALD-coated samples with Al_2O_3 and TaN, respectively. For samples 15 and 16, two NWs share common electrode gaps as indicated.

Sample	D_c (nm)	L_g (μm)	I_d	I_p	V_a (V)	I_{ALD} (A, T)	Batch/die
1	320	3.4	1.1 μA	5.4 μA	0.5	12.2 μA (A)	B738/F3 I-7-1
2	311	4.0	1.1 μA	11.4 μA	1	19.1 μA (A)	B738/F3 I-7-5
3	224	3.9	54 nA	1.6 μA	0.3		B738/T157 I-4-5
4	214	4.3	94 nA	4.7 μA	1	8.6 μA (A)	B738/F3 I-10-1
5	151	4.2	2.2 nA	1.7 μA	1		B738/T155 II-3-6
6	105	3.5	Noise	0.34 μA	1	1.1 μA (A)	B738/F3 I-6-1
7	108	3.8	Noise	0.29 μA	1		B738/P6 II-8-3
8	113	4.2	Noise	0.34 μA	−1	2.2 μA (A)	B738/F3 I-9-3
9	680	3.1	1.1 nA	0.13 μA	−4	2.4 μA (A)	B992/P8 I-8-4
10	147	7.3	Noise	30.6 nA	−4	34.6 nA(A)	B992/P8 II-9-3
11	160	4.8	Noise	1.0 nA	−4	10.0 nA(T)	B992/F8 II-1-7
12	172	5.8	Noise	1.0 nA	4	53.4 nA(A)	B992/P8 III-4-1
13	531	3.4	Noise	7.0 nA	−4	11.0 nA(T)	B992/F8 II-2-1
14	583	3.7	Noise	0.12 μA	4	2.2 μA (T)	B992/F8 I-6-7
15	160 76	3.4	Noise	0.33 μA	−1	0.87 μA(T)	B738/P5 I-1-1
16	200 150	4.5	Noise	16.6 nA	1	10.0 nA(T)	B992/F8 I-2-1

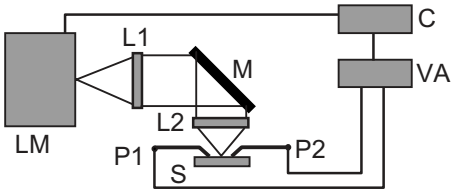

FIG. 2. Schematic of PC apparatus. The major components are as follows: LM: lamp/monochromator assembly, L1: collimating lens, M: turning mirror, L2: focusing lens, P1: electrical probe, P2: electrical probe, S: sample under test, VA: programmable current/voltage supply, and C: control computer.

B. Dark current and steady-state photocurrent in GaN NWs

The NW test structures were examined with a computer-automated current-voltage (*I-V*) probe apparatus that permitted simultaneous illumination in the visible-UV band while the *I-V* characteristics were being scanned and recorded. All measurements were performed at room temperature in ambient air. A schematic of the apparatus is illustrated in Fig. 2. The light source was a 75 W Xe arc lamp dispersed by a 150 mm focal length monochromator that operated with a spectral bandwidth of roughly 5 nm. The monochromator output was focused using fused silica optics to a maximum illumination intensity of $P(360)=3.6$ mW cm^{-2} for near/above-bandgap excitation of a sample under test. Higher UV intensities were provided by a HeCd laser operating at 325 nm which provided a maximum illumination intensity $P(325)=475$ W cm^{-2} with the optics available.

Starting first with a discussion of the thicker NWs that displayed nonzero dark current (Table I, samples 1–5, growth run B738), examples of the dark and steady-state PC behavior are now presented. A field emission scanning electron microscopy (FESEM) image of sample 1 is given in Fig. 3(a) and I_d-V (dark) and I_p-V [maximum $P(360)$ illumination] data for this sample are illustrated in Fig. 3(b). Graphs of I_p as a function of $P(360)$ and $P(325)$ for samples 3 and 5 are given in Figs. 3(c) and 3(d), respectively. The power intensity was varied by means of neutral density filters and the bias was 0.1 V in both cases. The bias was chosen to keep the maximum I_p from exceeding a few microamperes since devices would often fail at higher currents. The data illustrated in Fig. 3(c) indicate that I_p rises steeply with increasing illumination intensity until $P(325)\approx 10$ W cm^{-2}, but rises with significantly reduced slope thereafter. This effect is interpreted as a screening of the depletion field by photogenerated holes as follows.

The NW geometry offers a confinement structure that allows one to equate time resolved photoluminescence (TRPL) lifetime to minority carrier lifetime τ, as described by Ahrenkiel.[28] We have separately performed TRPL on NWs of comparable dimensions from these growth batches and typically find $\tau\approx 1$ ns in ambient air. The density of photogenerated holes n_{ph} under constant illumination intensity is given approximately by $n_{ph}\approx P(\lambda)\alpha(\lambda)\tau/\hbar\omega$. The absorption coefficient at 325 nm is given by $\alpha(325)\approx 1.2\times 10^5$ cm^{-1}.[29] For $P(325)=100$ W/cm^2, $n_{ph}\approx 2\times 10^{16}$ cm^{-3}. The data illustrated in Fig. 3(c) suggest that for

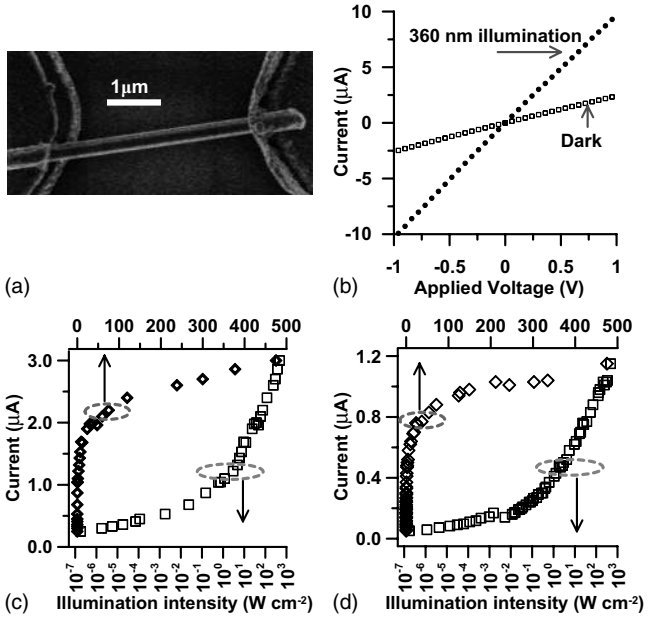

FIG. 3. (a) FESEM image of sample 1. (b) I_p-V and I_d-V for sample 1 under UV illumination (3.6 mW/cm^2 at 360 nm) and in the dark, respectively. (c) Combined graphs of I_p-$P(360)$ and I_p-$P(325)$ for sample 3 under a constant bias of 0.1 V. Illumination is at 360 nm for intensities $\leq$3.6 mW/cm^2 and at 325 nm for greater intensity levels. The same data are plotted on both linear and semilog scales in order to illustrate the transition to the regime where the depletion field is substantially screened. This is estimated to occur for $P(325)\approx 100$ W/cm^2. (d) Combined graphs of I_p-$P(360)$ and I_p-$P(325)$ for sample 5 under a constant bias of 0.1 V. Illumination scheme and simultaneous linear and semilog representation are the same as for (c). The transition to the regime where the depletion field is substantially screened is also estimated to occur for $P(325)\approx 100$ W/cm^2.

$P(325)\approx 100$ W/cm^2, n_{ph} becomes large enough to substantially screen the depletion field and allow the neutral conducting region to expand resulting in increased NW conductivity. This approximate analysis also reveals that the surface density of photogenerated holes available to screen the depletion field is $\approx 2\times 10^{11}$ cm^{-2} at this illumination intensity. As discussed in more detail below, for the samples considered in this study, a photogenerated surface hole density in the range of $(2-8)\times 10^{11}$ cm^{-2} should fully screen the depletion field so that $I_p\approx I_f$. However, a photoexcited hole density of roughly 2×10^{10} cm^{-2} should partially screen the depletion field such that I_p will fall within 90%–95% of I_f. Hence, we interpret the inflection illustrated in Fig. 3(c) where $P(325)\approx 1-10$ W/cm^2 as a transitional regime whereby for $P(325)<1$ W/cm^2, PC is dominated by partial screening of the depletion field by photogenerated holes while for $P(325)>10$ W/cm^2, the structure behaves more as a conventional photoconductor[30] in the sense that the density of photogenerated electrons becomes comparable or exceeds N_d with increasing $P(325)$. Similar behavior is seen for sample 5, as illustrated in Fig. 3(d), although this sample displays comparatively low dark current and is nearly depleted in the dark.

The representative behavior of the thinner NWs (depleted in the dark) from batch B738 is illustrated in Fig. 4(a) for sample 7. This figure illustrates I_p-V data for various constant values of $P(360)$. Figure 4(b) illustrates I_p for this sample under a constant bias of 0.8 V as a function of vary-

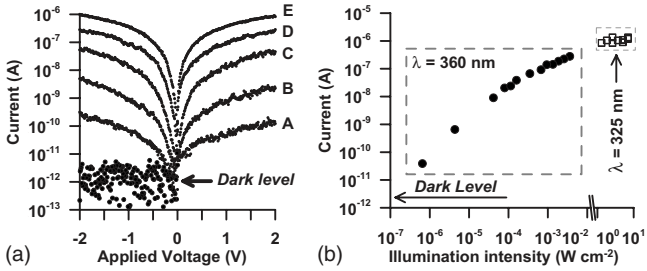

FIG. 4. (a) I_p-V for sample 7 at a wavelength of 360 nm taken at various values of illumination intensity. The magnitude of the current is plotted for negative voltage swings. A: 0.65 μW cm^{-2}, B: 4.3 μW cm^{-2}, C: 41.0 μW cm^{-2}, D: 0.35 mW cm^{-2}, and E: 3.6 mW cm^{-2}. (b) I_p-P(360) and I_p-P(325) for sample 7 under a constant applied bias of 0.8 V. Experimental limitations prevented attaining the maximum value for P(325) =475 W/cm^2 that was illustrated in Figs. 3(c) and 3(d).

ing levels of P(360) and P(325) up to a maximum of roughly $P(325) \approx 10$ W cm^{-2}. Experimental limitations precluded illuminating this sample at the maximum value of P(325) =475 W/cm^2 as described for samples 3 and 5. Sample 6 is an example of a bridge structure formed from a thinner NW. A FESEM image of this sample is shown in Fig. 5(a). The I-V characteristics under UV illumination and in the dark are shown in Fig. 5(b). The results illustrating the behavior of samples 6 and 7 are generally observed for the thinner NWs (whether they are bridge structures or lying flat on substrates), e.g., $I_p/I_d \approx 10^4-10^5$. Comparable photoconductive behavior in MBE grown c-axis GaN NWs depleted in the dark was also given by Calarco *et al.*[13]

The logarithmic scale used to display the magnitude of I_p in Figs. 4(a) and 5(b) partially obscures the fact that the I_p-V plots for the thinner NWs of this batch (samples 6–8) are sometimes asymmetric and not perfectly linear, whereas both the I_p-V and I_d-V behaviors of the thicker samples (samples 1–5) are usually perfectly linear. Precedent for this trend is also seen in the results of Ref. 13 for PAMBE grown GaN NWs that apparently contain a n-type background carrier concentration that is comparable to what we observe. We argue that this behavior is not unexpected in the thinner samples for the following reasons. Given the contact fabrication scheme, the portion of the NW beneath and in the immediate vicinity of the metal contact should be quite conductive as previously discussed. On the other hand, the portion of the wire extending away from the metal contact is fully depleted in the dark and partially depleted under UV excitation. Hence, a band offset should exist between the

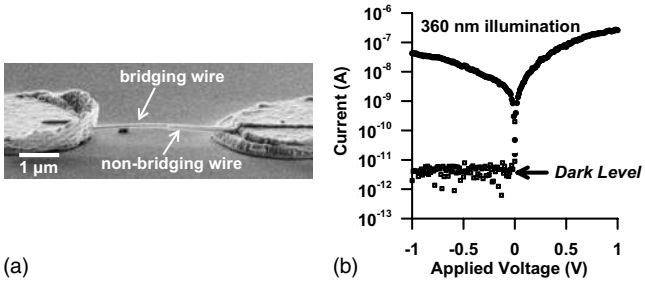

FIG. 5. (a) FESEM image of NW bridge (sample 6). The bridging NW is partially obscured by an adjacent nonbridging NW as indicated. (b). I_p-V and I_d-V for sample 6. UV illumination: 3.6 mW cm^{-2} at 360 nm.

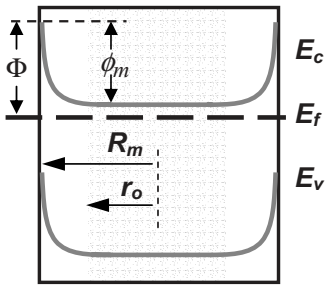

FIG. 6. Schematic of conduction and valence band bending for partially depleted cylindrical NW in the dark at equilibrium. The diameter $D_m = 2R_m$. The n-type NW contains a fully ionized donor density N_d. The surface supports a density N_s of ionized acceptors that trap conduction electrons, resulting in a cylindrically symmetric depletion region and upward bending bands. The Fermi level is "pinned" near midgap at the surface, as shown. The neutral region of the NW of diameter $2r_o$ that will conduct electrical current is indicated. The insulating depletion region supports the upward band bending shown. The maximum band bending of the conduction band between the undepleted region and the NW surface is defined as ϕ_m. The surface potential is defined by $\Phi_S = E_c - E_f$ evaluated at the surface, as shown.

more highly conductive GaN directly beneath the metal contact and the axially adjacent portion of the NW protruding away from the contact. Variations in contact processing conditions, slight tapering of the wires, etc., would lead to unequal barriers at either end of the NW. We speculate that the apparent partial Schottky-like behavior observed for some of the thinner NWs under UV illumination and the variation in I-V asymmetry with UV illumination intensity as seen in Figs. 4(a) and 5(b) may arise from these effects.

C. Analysis of steady-state dark current and photocurrent in GaN NWs

1. Cylindrical model to simulate depletion in NWs of hexagonal cross section

As illustrated in Fig. 6, we assume that the NW may be approximated by a cylinder of diameter D_m with uniform n-type doping density N_d leading to a free carrier concentration of the same density. The NW is partially or fully depleted by the presence of surface acceptor states of density N_s, resulting in an undepleted conducting neutral region of radius r_o within the wire. The maximum upward bending of the conduction band between the undepleted neutral region of the NW and the fully depleted surface is defined as ϕ_m. This convention should be distinguished from the surface potential Φ_S defined by $\Phi_S = E_c - E_f$ in a manner consistent with the usage of other authors.[13,31] An approximate expression for ϕ_m is derived by assuming an abrupt depletion boundary and using Gauss' law and the cylindrical symmetry to first calculate the radial electric field in the space-charge region and then computing $q\phi_m$, the work required to move a test charge from r_o to R_m. This simple temperature independent analysis gives

$$\phi_m = \frac{qN_d}{2\varepsilon}\left[\frac{R_m^2 - r_o^2}{2} - r_o^2 \ln\left(\frac{R_m}{r_o}\right)\right]. \quad (1)$$

In the preceding equation, $q = 1.602 \times 10^{-19}$ C and $\varepsilon = \varepsilon_o \varepsilon_r$, where $\varepsilon_o = 8.854 \times 10^{-14}$ F/cm and $\varepsilon_r = 8.9$.

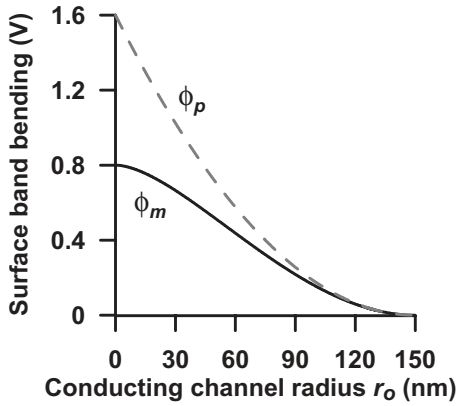

FIG. 7. Transcendental solution (solid line) of Eq. (1) showing an example of surface band bending ϕ_m as a function of conducting channel radius r_o (as defined in Fig. 6) for a presumed cylindrical NW with $N_d=7\times10^{-16}$ cm^{-3} and $R_m=150$ nm. The dashed line shows the surface band bending ϕ_p derived using the planar approximation that may be found in many books (Ref. 32). The figure illustrates that if ϕ_m is known from a separate measurement then r_o can be calculated for a NW that is not fully depleted provided the constraints of the temperature independent model surrounding the discussion of Eq. (1) are obeyed.

We mention that Eq. (1) is a special case of the more general (but still approximate) cylindrical analysis given by Dobrokhotov *et al.*[14] in their work on GaN NW gas sensors functionalized with metal nanoparticles. An example solution of Eq. (1) as a function of r_o is given in Fig. 7, where representative values $N_d=7\times10^{16}$ cm^{-3} and $R_m=150$ nm are used. Figure 7 also illustrates that the band bending becomes approximately parabolic as the depletion layer becomes thin compared with the NW diameter as expected from the standard planar depletion model.[32]

The upward bending of the conduction band for GaN surfaces has been estimated by electron photoemission, scanning Kelvin probe microscopy, and theoretical work.[31,33,34] From the results of those studies we expect that ϕ_m should fall somewhere in the range of roughly 0.1–1.1 eV. Additionally, Ref. 33 reports that there should be no significant difference in surface band bending between polar *c*-plane surfaces and nonpolar *a*-plane surfaces for MOCVD grown GaN films. Notably, the surface band bending for GaN can be strongly influenced by surface treatments[33] and Ga/N flux ratio in the case of MBE growth.[31] This latter point is significant for the present discussion since the PAMBE process that enables the NW growth morphology requires a much higher N to Ga flux ratio than what is typically used for conventional MBE growth of GaN films.[5] Given this range of estimates reported in the literature, there is no *a priori* reason to presume that ϕ_m for our samples that are examined in ambient air should be as high as 1.1 V, as reported in Ref. 33, or necessarily $\approx$0.55 V, as reported for the *c*-axis PAMBE grown GaN NWs in Ref. 13 since the latter are not grown under exactly the same conditions as ours.

Given its convenience and simplicity, one is particularly interested in the validity of Eq. (1) as $\phi_m \rightarrow kT/q$, and how well the cylindrical representation of the hexagonal NW cross section applies in this limit. We examined these issues as follows: A temperature dependent numerical Poisson solver applied to a NW geometry of hexagonal cross section was used to compute n_L (the integrated free charge per unit length of a NW) for the representative cases including $\phi_m=0.2$, 0.4, 0.6, 0.8 V; $N_d=4\times10^{16}$, 8×10^{16}, and 1.2×10^{17} cm^{-3}; and $D_i=220$, 280, 320 nm. In these simulations, the acceptor density N_s was taken as uniform over the NW surface and its value was adjusted to compute the values of ϕ_m just listed (at the tangential points where D_i intersects the hexagonal faces). The computed span of N_s ranged from 2×10^{11} cm^{-2} (smallest D_i, N_d, and ϕ_m) up to 8×10^{11} cm^{-2} (largest D_i, N_d, and ϕ_m).[35] Moreover, given the estimates of minority carrier lifetime and absorption coefficient previously discussed in the context of Figs. 3(c) and 3(d) we conclude that $P(325)$ in the range of 10^2–10^3 W/cm^2 should be sufficient to nearly or fully screen the depletion field over these representative spans of D_i, N_d, and ϕ_m. The simulation also reveals that ϕ_m is a strongly nonlinear function of N_s and for $N_s\approx2\times10^{10}$ cm^{-2}, the integrated free charge per unit length n_L is within 90%–95% of the flatband value. Thus we expect that a density of photoexcited holes n_{ph} of roughly 2×10^{10} cm^{-2} will yield $I_p\approx I_f$.

The span of values of ϕ_m and N_d listed in the previous paragraph was then used as input to calculate n_L by means of Eq. (1). In these calculations R_m was varied until the computed values of n_L equated with those obtained using the Poisson solver for the examples of D_i listed. D_m calculated in this fashion represents the diameter of an "equivalent" cylindrical NW and we label this diameter as D_m^e. We thus arrived at the values for D_m^e of $D_m^e=D_i+13\pm5$ nm, $D_i+10\pm3$ nm, and $D_i+9\pm4$ nm that correspond, respectively, to the three cases of N_d just listed. Hence, over this representative span of ϕ_m, N_d, and D_i, we find that $D_m^e-D_i\approx10$ nm. It is also instructive to compare the thickness of the depletion layer derived in the foregoing analysis to the effective Debye length L, where $L=\sqrt{\varepsilon kT/q^2N_d}$ (assuming that only donors are present).[36] Then another statement of the applicability range of Eq. (1) is that the depletion layer thickness $D_m^e/2-r_o$ should be greater than roughly four to five effective Debye lengths. Hence, the depletion in a NW of hexagonal cross section for the diameters considered can be reasonably represented by a cylinder of constant diameter D_m^e (with $D_m^e\approx D_i+10$ nm), and Eq. (1) is an approximate representation of the depletion in this structure provided that 0.2 V $\leq\phi_m\leq$0.8 V and 4×10^{16} cm$^{-3}\leq N_d\leq1.2\times10^{17}$ cm^{-3}.

2. Graphical analysis of steady-state dark current and illustration of uncertainties

The numerical problem for analyzing the steady-state dark conductivity in the NWs involves first examining samples with measurable dark current I_d and then calculating estimates of N_d, μ, and ϕ_m from

$$I_d=N_d\mu q\pi r_o^2V_d/L_g, \tag{2}$$

where L_g is the electrode gap and V_a is the applied voltage. Under the assumption that NWs from a common growth batch have common transport properties and surface band bending, one might expect that measurements of I_d from at least three separate NWs could allow for the unique determination of N_d, μ, and ϕ_m. In practice, however, this is not

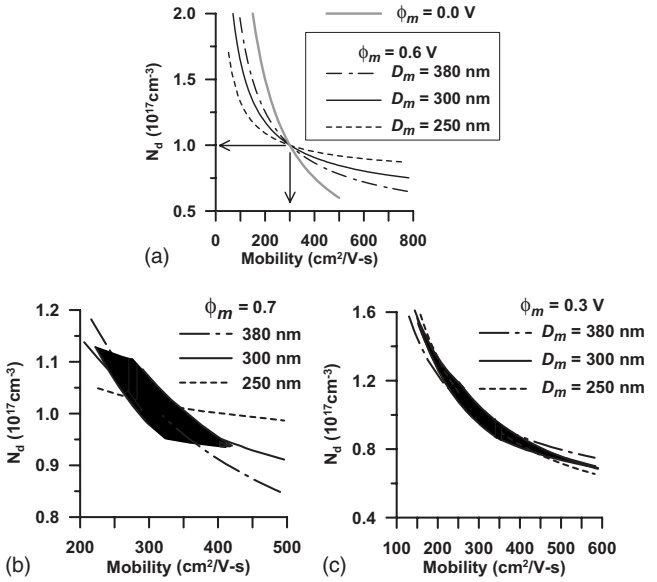

FIG. 8. (a) Graphs of N_d vs mobility computed from Eqs. (1) and (2) for three hypothetical NWs with diameters D_m as listed in the inset, $\phi_m = 0.6$ V, and each conducting known values of dark current I_d as given in the text. All three curves intersect at a common point corresponding to the input values of N_d and μ. Also shown is the collapse of the three curves to a single graph of N_d vs mobility when $\phi_m = 0$ V. (b) Graphs of N_d vs mobility computed as in (a) but with $\phi_m = 0.7$ V and the inclusion of an uncertainty in D_m of ± 10 nm for each NW. The shaded area illustrates the ambiguity in the common solution for N_d and μ for the three NWs. Hence, if the input values of I_d corresponded to measured data, the possible solutions for N_d and μ given the assumed value of ϕ_m and uncertainty in D_m cover the entire shaded area. (c) Graphs of N_d vs mobility computed as in (a) but with $\phi_m = 0.3$ V and the inclusion of an uncertainty in D_m of ± 10 nm for each NW. The result illustrates that the range of possible solutions of N_d and μ depends strongly on ϕ_m.

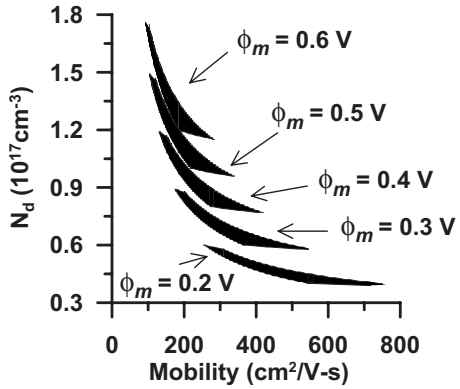

FIG. 9. Graphical solution for N_d vs mobility over a representative range of ϕ_m for samples 1–4 using the respective measured values of I_d and D_m as given in Table I. The uncertainty in D_m is accounted for by assigning the maximum and minimum values in diameter to those of cylinders that circumscribe and inscribe a NW of hexagonal cross section, as explained in the text.

feasible since the uncertainty in the measurements of the NW diameters is a significant limitation in this analysis as we now illustrate.

Consider three *hypothetical* two-terminal cylindrical NW structures with respective diameters $D_m^{1,2,3}=250$, 300, and 380 nm. We set $\phi_m=0.6$ V, $N_d=1\times10^{17}$ cm^{-3}, $\mu=300$ cm^2/(V s), $L_g=4$ μm, and $V_a=1$ V for each NW. Equations (1) and (2) may be used to numerically solve for the respective dark currents conducted in these wires, yielding $I_d^{1,2,3}=0.3868$, 1.4655, and 4.226 μA. Figure 8(a) illustrates the locus of solutions of Eq. (2) for N_d and μ corresponding to the input values of $I_d^{1,2,3}$ and the simultaneous solution conforming to the initially assigned values of N_d and μ. Also illustrated in the figure is the computed flatband condition where $\phi_m=0$ and $r_o=R_m$ for each NW, yielding solutions that are necessarily degenerate for the three cases. In Fig. 8(b) we use $\phi_m=0.7$ V and illustrate the locus of permissible solutions for N_d and μ when an uncertainty in diameter $\delta D_m=\pm10$ nm for each NW is included. This results in a range of possible simultaneous solutions of equal probability with N_d spanning roughly from 0.94 to 1.12 $\times10^{17}$ cm^{-3} and μ spanning roughly from 225 to 425 cm^2/(V s). The possible solutions for N_d and μ also depend strongly on ϕ_m, as illustrated in Fig. 8(c), where we show an additional example resulting from $\phi_m=0.3$ V. Thus, under the assumption that the cylindrical representation of a NW is accurate, the "correct" values for carrier concentration and mobility, i.e., $N_d=1\times10^{17}$ cm^{-3} and $\mu=300$ cm^2/(V s), cannot be recovered without significant error even when the δD_m is only a few percent of the NW diameter. We now apply these graphical methods to estimate ranges of N_d and μ for samples described in Table I that displays nonzero dark current, and then check the consistency of the results with the observed photocurrent.

In Fig. 9 we illustrate the result for samples 1–4 where a representative span in ϕ_m from 0.2 to 0.6 V is considered. Table I gives the corresponding values of I_d, V_a, L_g, and D_c used as input for each sample in the calculation. We consider the maximum uncertainty in diameter by calculating results using estimated minimum and maximum values of diameter for each sample. The extrema in D_m are estimated as follows: FESEM was used to measure D_m in plan view. The NWs typically rest with a hexagonal facet in contact with the substrate (or bottom electrode pad). Thus, $D_m \approx D_c$, and values of D_c appearing in Table I correspond to such estimated maxima. The estimated minimum NW diameters D_i correspond to inscribed cylinders as defined earlier. As shown in Fig. 9, when this estimated maximum uncertainty in the NW diameter is taken into account, the measured values of I_d for growth batch B738 can be accommodated over the given representative range of ϕ_m with μ spanning from roughly 100 to 750 cm^2/(V s) and the corresponding range of N_d spanning from 1.8×10^{17} down to 4.0×10^{16} cm^{-3}. Note that Table I also includes sample 5 that exhibits the lowest nonzero I_d of batch B738. However, since this sample is relatively close to depletion, it is poorly simulated by Eq. (1) and its measured value of I_d does not map onto Fig. 9 using the procedure just described. The samples of batch B992 cannot be analyzed by this procedure since there is only sample 9 thick enough ($D_c=680$ nm) to permit nonzero I_d. The experimental results obtained from batch B992 suggest that N_d for this batch should be roughly ten times less than for the B738 sample set. This point will be discussed further in Sec. II E.

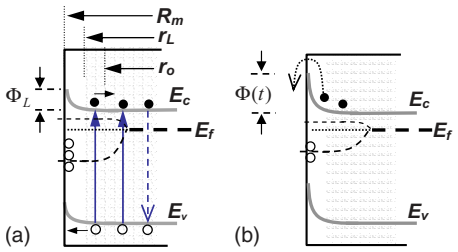

FIG. 10. (Color online) (a) Schematic showing the reduction in surface band bending from the equilibrium dark value ϕ_m to Φ_L under steady UV excitation. Upward arrows indicate photogeneration of electron-hole pairs; the downward arrows indicate aggregate electron-hole recombination via radiative and nonradiative pathways. Photoexcited holes drift to the surface of the NW under the action of the depletion field and become trapped, thereby partially screening the ionized acceptor states and reducing the surface band bending. This nonequilibrium situation is depicted schematically by separate effective Fermi levels for electrons and holes, as illustrated. The radius of the neutral conducting region in the dark r_o increases to r_L under UV illumination, yielding increased conduction of the NW. (b) Schematic showing the transient recovery of the surface band bending following cessation of UV illumination. Conduction electrons surmount the barrier $\Phi(t)$ by thermionic emission and recombine with trapped holes at the surface. As the process continues, $\Phi(t)$ eventually returns to the dark equilibrium value ϕ_m.

D. Analysis and simulation of persistent photocurrent decay

1. Development of model

An approximate model for the time decay of the persistent photocurrent $I_p(t)$ is now developed. Our approach is motivated by the work of Reshchikov *et al.*[37] in their study of UV-induced transient photovoltage in planar GaN films. Under uniform above-bandgap illumination, photogenerated holes are swept to the NW surface by the depletion field and trapped. This accumulation of holes on the surface effectively compensates the negatively charged surface acceptors and reduces the upward bending of the conduction band to Φ_L, where $\Phi_L < \phi_m$. The NW becomes less depleted, and the radius of the neutral region increases to r_L with $r_o < r_L < R_m$. This nonequilibrium situation is depicted in Fig. 10(a). When the illumination is ceased, an instantaneous initial persistent current I_p^o flows and the total initial current in the NW is $I_p^o + I_d$. Recombination occurs via electrons at the bottom of the conduction band in the neutral region surmounting the surface barrier Φ_L by thermionic emission and recombining with the holes trapped at the surface, as illustrated in Fig. 10(b). The surface band bending increases with time as $\Phi(t)$, the radius of the neutral region decreases with time as $r_o(t)$, $I_p(t)$ decreases from its initial value of I_p^o, and the recombination rate slows because the increasing $\Phi(t)$ results in a greater barrier to thermionic emission. This approximate model neglects other possible trap states, tunneling of carriers through the surface barrier, and additional radiative and nonradiative recombination pathways that may exist. As the dark equilibrium state is restored, $\Phi(t) \to \phi_m$, $r_o(t) \to r_o$, $I_p(t) \to 0$, and the current returns to I_d. The rate of electron-hole recombination may be expressed as

$$\frac{dp_s(t)}{dt} = -p_s(t) C_n N_d \exp\left(-\frac{\Phi(t)}{kT}\right). \tag{3}$$

In the preceding equation p_s is the time dependent photogenerated hole density at the surface, C_n is the electron-hole capture coefficient, and the density of thermally activated electrons from the bottom of the conduction band in the neutral region of the NW that is available for surface recombination is given by N_d multiplied by the Boltzmann factor. C_n is related to the capture cross section σ_n by the relation $C_n = \sigma_n \sqrt{8kT/\pi m_n}$, where m_n is the effective mass of conduction band electrons and $m_n = 0.20 m_e$, yielding $C_n = \sigma_n 2.4 \times 10^7$ cm/s.[37]

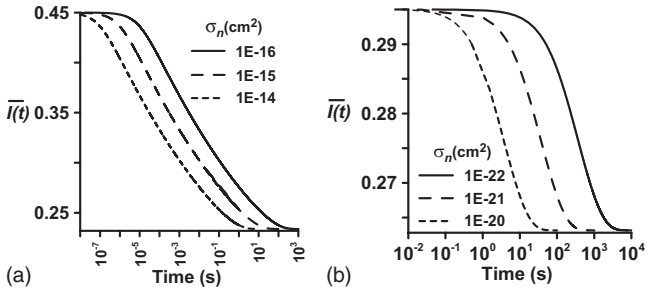

FIG. 11. (a) Hypothetical photoconductive decay computed from Eq. (4) with $D_m = 200$ nm, $N_d = 3 \times 10^{17}$ cm^{-3}, $\phi_m = 0.65$ V, and three values of capture cross section σ_n: 10^{-16}, 10^{-15}, and 10^{-14} cm^2. The result is comparable with a similar treatment of transient surface photovoltage given in Ref. 37. (b) Hypothetical photoconductive decay computed from Eq. (4) with $D_m = 350$ nm, $N_d = 5 \times 10^{16}$ cm^{-3}, $\phi_m = 0.3$ V, and three values of σ_n: 10^{-22}, 10^{-21}, and 10^{-20} cm^2.

Equation (3) is readily put into a form amenable to numerical simulation with the following arguments. From the requirement of charge neutrality between the surface and the depletion region, the steady-state density of ionized surface acceptors in the dark may be expressed as $N_S = (N_d/2R_m) \times (R_m^2 - r_o^2)$. Similarly, the steady-state population of ionized surface acceptors under constant illumination is $N_S^L = (N_d/2R_m)(R_m^2 - r_L^2)$. Thus, the steady-state population of photoexcited holes under constant illumination is $p_o^L = N_S - N_S^L$. When the illumination ceases, the time dependent population of photoexcited holes is then $p(t) = N_S - N_S(t)$. The time dependent undepleted cross sectional area of the NW arising from photoexcitation is defined as $A(t)$, where $A(t) = \pi(r_o^2(t) - r_o^2)$. Thus $p(t) = N_d A(t)/(2\pi R_m)$ and Eq. (3) is recast as

$$\frac{dA(t)}{dt} = -A(t) C_n N_d \exp\left(-\frac{\Phi(t)}{kT}\right). \tag{4}$$

The time dependence of the surface band bending $\Phi(t)$ is obtained from Eq. (1) with r_o replaced by $\sqrt{r_o^2 + A(t)/\pi}$. Clearly $I_p(t) = N_d \mu q A(t) V_a / L_g$ so that the solution of Eq. (4) is proportional to the time decay of the persistent photocurrent. Equation (4) is solved numerically using an adaptive step fourth-order Runge–Kutta algorithm. The specific Runge–Kutta coefficients used are given by Carnahan *et al.*[38]

To put this into context, we compute example solutions of Eq. (4) representing the time decay of normalized persistent photocurrent for an undepleted NW where N_d, ϕ_m, and σ_n conform to values of these parameters used in the analysis of transient photovoltage for planar GaN films presented in Ref. 37. These results are illustrated in Fig. 11(a) where $D_m = 200$ nm, $N_d = 3 \times 10^{17}$ cm^{-3}, $\phi_m = 0.65$ V, and three values for capture cross section σ_n are used (10^{-16}, 10^{-15}, and 10^{-14} cm^2). The model is not expected to apply when [R_m

$-r_o(t)] < 4-5L$; thus, we calculate that the initial condition at which Eq. (4) should reasonably represent the decay of normalized photocurrent $\bar{I}(t)$ in this example starts at the point where $\bar{I}(t=0) \approx 0.45$ and $[r_o(t)/R_m]^2 = [I_p(t)+I_d]/I_f \equiv \bar{I}(t)$. Both our model and that of Ref. 37 can be viewed as similar; however, there are some clear distinctions. Within the constraints previously discussed, our model solves for the full time dependent evolution of the surface band bending for a GaN cylinder and the corresponding time dependent cross sectional area of the neutral region. By contrast, Ref. 37 finds the time evolution for the surface band bending for a planar GaN film within the approximation that the photoinduced variation in band bending is small compared to the dark surface band bending. Hence, one would expect similar, but not directly comparable results for the same input values of N_d and σ_n applied to both situations. In particular, in Fig. 11(a) we find that the persistent photocurrent should decay in roughly 50–100 s when $\sigma_n = 10^{-15}$ cm^2 which is qualitatively consistent with the temporal evolution of surface band bending, as calculated in Ref. 37. As a second example, Fig. 11(b) illustrates the case for $D_m = 350$ nm, $N_d = 5 \times 10^{16}$ cm^{-3}, and $\phi_m = 0.3$ V, and σ_n in the range from 10^{-22} to 10^{-20} cm^2 are used. The starting time of the simulation was adjusted to account for constraint imposed by L as previously described. Of course our key task is to consider the inverse problem, i.e., fitting the simulation to the photocurrent decay data in an effort to solve for N_d and σ_n. The ideal uniqueness of these fitted solutions is discussed in the Appendix.

Fitting the temporal decay of the persistent photocurrent for wires with nonzero I_d offers a means to further restrict the estimated acceptable ranges of N_d and μ as follows. For a given NW with measured I_d, I_p^o, $I_p(t)$, and D_c, the ratio of dark current to flatband current is given by $I_d/I_f = (r_o/R_e^f)^2$. From the earlier estimates of the range of n_L is necessary to attain 90%–95% of flatband conditions, and using Figs. 3(c) and 3(d), I_f falls into the approximate range of $2.5I_p < I_f < 5I_p$. The resulting span of I_p/I_f is then 0.2–0.4, and we may compute the corresponding bounds on $r_o(t)$ given I_d and D_c. Using these quantities and D_m^e, we vary N_d and σ_n in a least-squares minimization procedure to fit Eq. (4) to $\bar{I}(t)$ for the case at hand.

2. Analysis of samples from batch B738

Figures 12(a)–12(d) illustrate fitting the decay of $\bar{I}(t)$ for samples 1 and 2. Here the data were normalized and the start times t_o for the simulations were constrained as previously described. The start time of the simulation shown in Fig. 12(a) for sample 1 (the thickest samples from batch B738) occurred at $t_o = 0$ (at the start of the actual photoconductive decay) under the assumption that $\bar{I}(t=0) = 0.2$. In Fig. 12(b), however, the fit of the same data was performed for $\bar{I}(t=0) = 0.4$ and t_o was necessarily delayed until $\Phi(t)$ had recovered sufficiently such that the cylindrical depletion model was valid. Figures 12(c) and 12(d) show similar fitting of $\bar{I}(t)$ data for sample 2. Analysis of samples 3 and 4 gives similar results but utilizes less of the available data since t_o must be delayed further in order to accommodate the limitations of

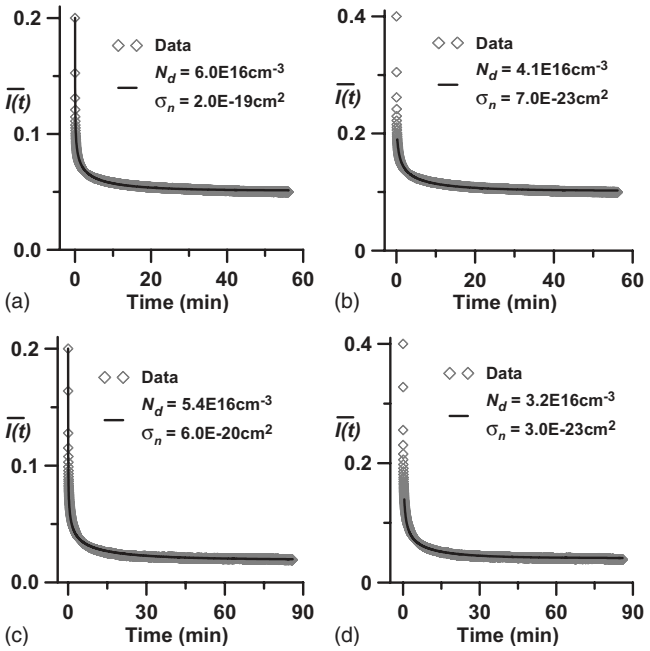

FIG. 12. (a) Fit of the simulated photoconductive decay to the data of sample 1 is shown as the solid line and the normalized data are shown as open symbols. The start time of the simulation conforms to the start of the photoconductive decay in the approximation that $\bar{I}(t=0) = 0.2$. The optimum solution is found for $N_d = 6.0 \times 10^{16}$ cm^{-3} and $\sigma_n = 2.0 \times 10^{-19}$ cm^2. (b) Fit of the simulated photoconductive decay to the data of sample 1 in the approximation that $\bar{I}(t=0) = 0.4$. This yields $N_d = 4.1 \times 10^{16}$ cm^{-3} and $\sigma_n = 7.0 \times 10^{-23}$ cm^2. (c) Fit of the simulated photoconductive decay to the data of sample 2 in the approximation that $\bar{I}(t=0) = 0.2$, yielding $N_d = 5.4 \times 10^{16}$ cm^{-3} and $\sigma_n = 6.0 \times 10^{-20}$ cm^2. (d) Fit of the simulated photoconductive decay to the data of sample 2 in the approximation that $\bar{I}(t=0) = 0.4$, yielding $N_d = 3.2 \times 10^{16}$ cm^{-3} and $\sigma_n = 3.0 \times 10^{-23}$ cm^2.

the depletion approximation imposed by these progressively thinner samples. Sample 5 is too thin to apply the model even though its $I_d \neq 0$.

The simulations reveal that the estimated uncertainty in setting the normalization of $I_p(t)$ results in the fitted solutions for N_d and σ_n spanning roughly $(3-6) \times 10^{16}$ cm^3 and $10^{-23}-10^{-19}$ cm^2, respectively. These results for N_d taken together with the (dark) current-voltage data presented in Fig. 9 suggest that μ should fall in the range of roughly 500–700 cm^2/(V s). This result is consistent with our prior assertion that μ for UID MBE grown GaN NWs should be comparable to μ extrapolated from Hall mobility data reported for crack-free MBE GaN films with comparable n-type background that was grown on Si(111).[26]

The fully depleted NWs from this batch (samples 6–8 with D_c spanning 105–113 nm) typically showed faster photoconductive decay [as illustrated in Fig. 13(b), sample 8, for the case of no ALD coating]; however, these samples are too thin to permit fitting the simulation to the data using the foregoing procedure. The I_p versus $P(360)$ data illustrated in Fig. 4(b) for sample 7 is generally representative of these depleted NWs from this batch and we again expect that I_p is within 90%–95% of I_f for $P(325) = 10$ W/cm^2 and that $0.2I_f < I_p < 0.4I_f$ for $P(360) = 3.6$ W/cm^2.

According to Ref. 37, our estimated range of σ_n ($10^{-19}-10^{-23}$ cm^2) should be comparatively low for semi-

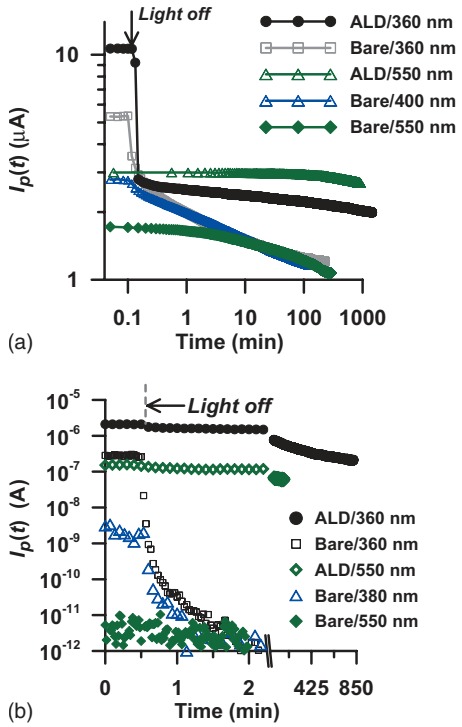

FIG. 13. (Color) (a) Comparative PPC of sample 1 before ("Bare") and after ("ALD") coating with roughly 10 nm of ALD deposited Al_2O_3. The corresponding excitation wavelengths are indicated. (b) Comparative PPC of sample 8 before ("Bare") and after ("ALD") coating with roughly 10 nm of Al_2O_3. The corresponding excitation wavelengths are indicated.

conductors; however, even smaller values ($\approx 10^{-25}$ cm^2) have been reported in pulsed voltage studies of Si surfaces subjected to various etchants.[39] Moreover, Hirsch *et al.*[40] in their study of photoconductive decay in ≈ 3 μm thick GaN films with $N_d = 1 \times 10^{17}$ cm^{-3} reported room temperature decay times of roughly 10^3 s, inferred a capture barrier of ≈ 0.2 eV, and remarked that the capture cross section must be "extremely small." If we interpret their room temperature data as arising from the mechanism whereby the variation in surface depletion thickness accounts for the photoinduced few percent variation in conductivity, then given a decay time of 10^3 s and associating their capture barrier with our ϕ_m, we estimate that their capture cross section is on the order of 10^{-26} cm^2. The variation in conductivity they reported is not unexpected using our model since the depletion layer thickness in the dark under these conditions would be roughly 44 nm, i.e., within a few percent of the film thickness.

E. Effects of ALD coating on NW conductivity and examples of below-gap PC behavior

Figures 13(a) and 13(b) illustrate the comparative photoconductive behavior under illumination at 360, 380, 400, and 550 nm for samples 1 and 8 before and after these devices were conformally coated with roughly 10 nm of Al_2O_3 by ALD. ALD coating was performed using trimethylaluminum and H_2O as the reactants.[41–43] There are significant distinctions to note in comparing PC and PPC before and after ALD coating. For example, prior to Al_2O_3 coating, we generally found relatively weak subgap PC which would become more prominent after ALD coating. Additionally, the decay rate of the persistent current for a given device prior to coating was comparable for all illumination wavelengths that yielded PC, even though, as seen in Figs. 13(a) and 13(b), there was a considerably reduced photoresponse for the excitation wavelengths greater than 360 nm. However, after Al_2O_3 coating, the photoconductive response at all excitation wavelengths and the decay time were substantially increased.

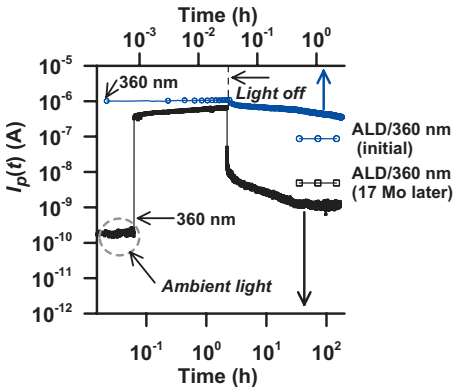

FIG. 14. (Color) Comparative PPC of ALD Al_2O_3 coated sample 6. Initial 4 h PPC scan following UV excitation was recorded 1 month following ALD coating. Follow-up PPC scan under ambient light and UV excitation was recorded 17 months later. The sample was stored in ambient light and not exposed to UV between the two scans.

An example of the long-term aging behavior of PPC for sample 6 coated with Al_2O_3 is illustrated in Fig. 14. Prior to ALD coating, this sample showed no measurable photocurrent under ambient light illumination. The photoconductive decay time for this sample prior to ALD coating was comparable to that displayed by sample 8 in Fig. 13(b). UV PC experiments were performed on sample 6 roughly 1 month after the ALD coating. It was then stored for 17 months in ambient light conditions. Figure 14 illustrates the UV photoresponse and PPC decay recorded within 1 month of ALD coating and the photoconductive behavior taken after 17 months. The latter starts with the photocurrent recorded under ambient light, as shown, followed by exposure to UV light. When the UV light was switched off, the PPC decay in the dark was initially much faster than that illustrated in the initial experiment. However, the photocurrent measured under ambient light conditions is not recovered after 7 days of monitoring $I_p(t)$ in the dark. Figures 15(a) and 15(b) illustrate comparative PPC under 360 nm exposure before and after ALD Al_2O_3 coating of samples 9 and 10 from growth batch B992; they show that the Al_2O_3 coatings produces a comparable change in behavior of photoconductive response for NWs from both growth runs.

Table I tabulates data for I_p [photocurrent for $P(360) = 3.6$ W/cm^2 before ALD coating] with I_{ALD} [photocurrent for $P(360) = 3.6$ W/cm^2 after ALD coating] for samples from batch B738. Combining these results with the previous estimates of I_f for these samples reveals that the effect of ALD Al_2O_3 coating increases the photocurrent such that $I_{ALD} \approx I_f$ for $P(360) = 3.6$ W/cm^2. ALD Al_2O_3 has been reported to introduce interface trap states for GaN whose density depends on processing and annealing conditions.[44] Our results showing increased conductivity and a slowing of the

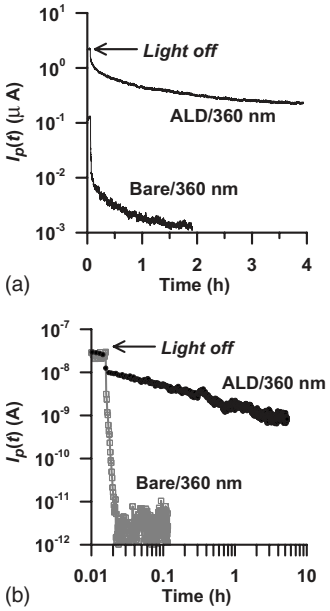

FIG. 15. (a) Comparative PPC under UV illumination before and after ALD Al_2O_3 coating of sample 9. (b). Comparative PPC under UV illumination before and after ALD Al_2O_3 coating of sample 10.

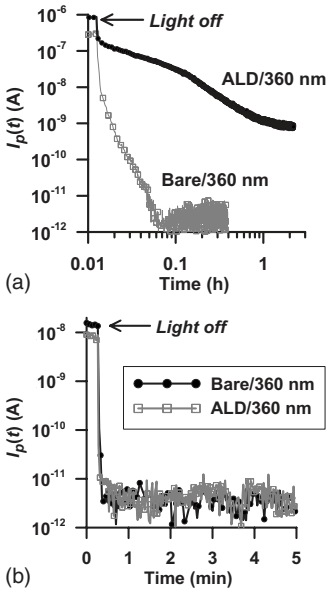

FIG. 16. (a) Comparative PPC under UV illumination before and after ALD TaN coating of sample 15. (b) Comparative PPC under UV illumination before and after ALD TaN coating of sample 16.

decay rate of PPC in the Al_2O_3-coated NW devices suggest that the oxide layer introduces long-lived hole traps such that the surface band bending is substantially reduced under UV illumination and recovers far more slowly (if at all) in the dark compared to the uncoated cases. By contrast, studies of comparative PPC on GaN NWs under vacuum and exposed to air suggest that adsorbed oxygen plays a role in accelerating PPC decay.[45]

We generally observe consistent conductivity and PC behavior for NWs taken from a single growth run but differences in behavior between growth runs. On the other hand, the low strain and defect-free nature of the NWs is maintained from run to run. Such trends were evident for the two UID *n*-type sample batches considered in this paper and for the study of Si-doped *n*-type NWs published separately.[20] We would expect differences in UID *n*-type behavior between sample batches because it is difficult to duplicate exactly the same PAMBE growth conditions between growth runs. Furthermore, one would expect that such differences would become more evident for samples with relatively low background carrier concentration. Drawing from our earlier arguments based on the high structural quality of these NWs, μ for batch B992 should also be in the range of 500–700 $cm^2/(V\ s)$. Furthermore, when these wires were ALD coated with Al_2O_3 we would also expect that $I_{ALD} \approx I_f$ for $P(360)=3.6\ W/cm^2$. Taken together, these estimates are consistent with $N_d \approx 5\times10^{14}-1\times10^{15}$ for this wire batch.

Other ALD coating schemes were also explored on both sample batches. We performed comparative 360 nm PPC experiments on NW devices (samples 11 and 13–16) before and after they were coated with roughly 7 nm of TaN by ALD. The coating was performed using (*tert*-butylimido)tris(diethylamido) tantalum and hydrazine as the reactants.[46] The results are summarized in Table I. Figures 16(a) and 16(b) illustrate the respective results of PPC decay for samples 15 and 16. Since the intent of these TaN coating experiments was to obtain a qualitative comparison with the Al_2O_3 ALD-coated samples, we did not take extra steps to ensure that all test structures supported only a single NW between the electrodes. Figure 16(a) shows the PPC behavior for sample 15 consisting of two NWs from batch B738 (with approximate diameters of 76 and 160 nm) that bridged a common electrode gap of 3.4 μm with −1 V dc bias applied. The observed photocurrent prior to ALD coating was consistent with only the thinner wire conducting under UV illumination. The TaN ALD-coated sample shows increased PPC compared to the bare sample, but the effect is far less than that illustrated in Fig. 13(b) for Al_2O_3-ALD-coated samples of comparable diameter from the same growth batch. Figure 16(b) illustrates the results for sample 16 consisting of two bridging wires (with approximate diameters of 150 and 200 nm) taken from batch B992, where the electrode gap was 4.5 μm and +1 V dc bias was applied. In this case we found that the effect on the PPC of the TaN ALD coating was essentially negligible. As noted in Table I, samples 11, 13, and 14 all showed an increase in peak PC after ALD TaN coating, but we did not observe any significant change in the PPC decay time compared to that for the uncoated state of these samples.

Finally, we remark that control experiments were performed to check for possible conductivity and PC in both the Al_2O_3 ALD and TaN ALD films. In these experiments, the electrical continuity before and after ALD coating was checked between contact pads that were devoid of any connecting NWs. In no case was conductivity or PC of the ALD deposited films resolved within the sensitivity of our measurements.

III. DISCUSSION

Measurement of transport properties in semiconductor NWs often involves the fabrication of FET devices and esti-

mation of carrier concentration and mobility from the conductance and pinch-off conditions.[47] Some authors have cautioned that the results of such analyses will depend strongly on the sophistication of the simulation tools and the model employed.[48] Our own observations of drift and hysteresis in NW FET devices further illustrate that the application of sophisticated simulation tools does not necessarily guarantee reliable extraction of transport properties.[16,20,49] The methods presented herein offer an alternative approach for estimating N_d, μ, and ϕ_m and require the fabrication of relatively simple two-terminal NW devices rather than three-terminal FET structures. The combination of the *I-V* and time decay measurements offers a useful "cross-check" since the latter do not depend on mobility. However, for the dark *I-V* measurements, one must employ a range of NW diameters such that the set of samples spans from fully depleted in the dark to substantially undepleted while at the same time conforming to the limitations in the depletion approximation as described earlier. Of course, abandoning the convenience and simplicity offered by the cylindrical depletion model of Eq. (1) and employing a fully temperature dependent numerical solution scheme should improve results. Nonetheless, selection of a sufficient span of D_c is still required and could prove challenging depending on the doping level and growth conditions. Indeed, as described above, for a doping level in the range of 10^{14}–10^{15} cm^{-3}, it was difficult to find NWs thick enough to yield nonzero dark current. On the other extreme, a *n*-type GaN NW doped at $\approx 10^{18}$ cm^{-3} with $\phi_m = 0.3$ V would be completely depleted for $D_m \approx 50$ nm, and the growth conditions may not yield a sufficient distribution of diameters in this range.

The simulations of photoconductive decay illustrate that relatively small uncertainties in N_d (factors of 2) can result in much larger uncertainties in σ_n. Consequently, it is difficult to directly compare our estimated results for σ_n with those of Ref. 37 even though the formal analysis is quite similar. Additionally, the uncertainty encountered in setting the normalization of the photocurrent decay compounds these problems, as illustrated in Figs. 12(a)–12(d). Therefore, the theoretically obtainable fits that should return unique values of N_d and σ_n, as described in the Appendix, are not obtained in practice; however, one can use this analysis to place bounds on these quantities. In this manner we were able to estimate that 3×10^{16} $cm^{-3} < N_d < 6 \times 10^{16}$ cm^{-3} for batch B738 and then use the data of Fig. 9 to determine that μ should fall into the range of 500–700 $cm^2/(V\,s)$ as one might anticipate for low defect density MBE grown GaN.[26]

We acknowledge the possibility that variations in carrier concentration between wires or within wires from a single growth run could certainly exist. However, the general trends illustrating the variation in conductivity with diameter (both herein and in Ref. 20) suggest that this is a secondary effect if it occurs.

The subgap PC was observed on samples before and after ALD coating with Al_2O_3. The intensity illuminating the samples at these wavelengths (380, 400, and 550 nm) was within a factor of 2–3 of that available at 360 nm. Several minutes were typically required for the photocurrent to reach equilibrium under constant illumination at these wavelengths. By contrast, PC under 360 nm illumination would generally rise to a maximum level within a few seconds for uncoated NWs. Figures 13(a) and 13(b) illustrate that the decay time of the PPC was comparable for all excitation wavelengths prior to ALD coating. This suggests that the same decay process (e.g., photogenerated holes trapped on the surface recombining with conduction electrons thermionically emitted from the neutral region) is responsible in all cases. Armstrong *et al.*[18] argued that subgap PC should be dominated by majority carrier photoemission from a deep level within the depletion region. Here, the photogenerated electron emitted into the conduction band would be pulled into the neutral region and the remaining positive charge would partially screen the depletion field since it is in the immediate vicinity of the surface.

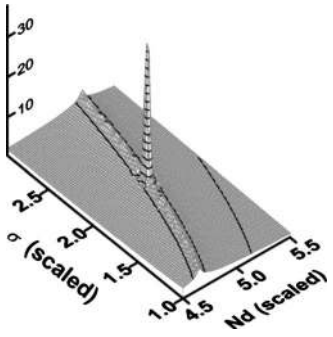

FIG. 17. 3D map of the least-squared solution of Eq. (4) using as input data the hypothetical case illustrated in Fig. 11(b) with $D_m = 350$ nm, $N_d = 5 \times 10^{16}$ cm^{-3}, and $\sigma_n = 1 \times 10^{-21}$ cm^2. The map is scaled such that N_d ranges from 4.5×10^{16} to 5.5×10^{16} cm^{-3} and σ_n ranges from 5×10^{-22} to 1.48×10^{-21} cm^2. The vertical axis is the negative logarithm of the least-squared deviation between the input and computed normalized photoconductive decay and is arbitrarily truncated at a value of 30. The pole conforms to a solution coincident with the values of N_d and σ_n used to generate the input data. The locus of minima appearing as a continuous "ridge" traversing diagonally across the map conforms to the solution of the limiting case where $\Phi(t) \rightarrow \phi_m$.

If this mechanism were dominant we would not necessarily expect the same decay time as observed for 360 nm excitation nor would we expect to see an increase in decay time following ALD coating. However, uncoated NWs show roughly the same PPC decay times when excited above or below gap and PPC decay times always increase after ALD Al_2O_3 coating for all excitation wavelengths considered. These observations suggest that the surface plays the dominant role and that subgap excitation produces mobile holes via transitions to intermediate trap and/or defect levels. This process would first involve majority carrier photoemission of a deep level, as suggested in Ref. 18, followed by photoexcitation of an electron from the valence band to the same deep level, thus leaving a mobile hole available to be swept to the surface and participate in screening the depletion field.

While such defect/trap states plausibly explain the observed subgap PC within the context of our model, we saw no evidence of midgap "yellow band" PL from these NWs.[50] PL was performed at 16 and 300 K on samples 2, 4, 6, and 8 (prior to Al_2O_3 ALD coating) and on other various single NW samples from both growth runs before and after ALD alumina coating.[8] In no cases did we observe below-gap PL emission. Finally, we also remark that we do not observe

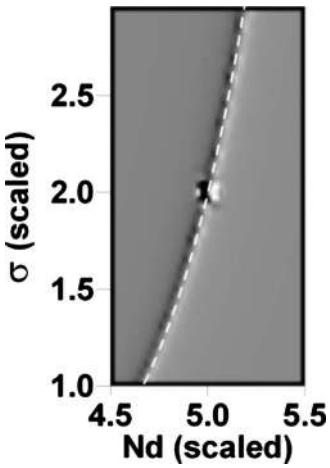

FIG. 18. Plan view shaded relief of the 3D map of Fig. 17. As explained in the text, the superimposed dashed line is a separate solution of the limiting case $\Phi(t) \rightarrow \phi_m$ represented by a solution of Eq. (A1).

sensitivity of the photocurrent to polarization of the excitation light, as has been reported in other GaN NW photoconduction studies.[51]

IV. CONCLUSIONS

Combined metrology methods involving current-voltage measurements, PC, and transient PC offer a means to estimate carrier concentration, band bending, drift mobility, and depletion layer thickness in GaN NWs. The results illustrate that primary sources of uncertainty in these studies are measurements of the diameters of the NW samples and estimates of the relative magnitude of the steady-state photocurrent with respect to the maximum flatband current. The methodology requires an ensemble of uniform individual NWs spanning various diameters such that samples range from ones that are nearly depleted in the dark to ones that are strongly conductive in the dark. An additional constraint is that the depletion layer thickness should be greater than four to five effective Debye lengths in order for the simple temperature independent cylindrical depletion model to be valid. For NW samples from a single growth run that conformed to these constraints, we found that UID *n*-type free carrier concentration, surface band bending, and electron drift mobility fall into the approximate respective ranges of $(3-6) \times 10^{16}$ cm^{-3}, 0.2–0.3 V, and 500–700 cm^2/(V s). A second set of more heavily depleted NWs from a separate growth run with an estimated 10–100 times lower free carrier concentration could not be fully analyzed by these methods. NWs were driven to apparent flatband conditions by continuous 325 nm illumination at intensities near or exceeding 100 W/cm^2. ALD Al_2O_3 coatings were found to strongly increase the PC such that nearly flatband conditions could be attained at substantially lower illumination intensities. By contrast, TaN ALD coatings were found to have less perturbation on the conductivity properties.

ACKNOWLEDGMENTS

We gratefully acknowledge fruitful conversations with Professor Benjamin Klein of Georgia Institute of Technology-Savannah regarding comparisons of our cylindrical depletion model with numerical simulations of the true NW hexagonal cross section. Additionally, we have benefited from collaboration with Christopher Dodson and Joy M. Barker (now at Sandia National Laboratory) during her tenure at NIST as an NRC-sponsored postdoctoral fellow. This work received partial support from the DARPA Center for Integrated Micro/Nano-Electromechanical Transducers (*i*MINT) funded by DARPA S&T Fundamentals Program (Award No. HR0011-06-1-0048).

APPENDIX: DISCUSSION OF THE UNIQUENESS OF THE PHOTOCONDUCTIVE DECAY FITTING PROCEDURE

We examine the problem of fitting photoconductive decay data as a method to recover unique values of N_d and σ_n. This is motivated by the concern that as the decay approaches equilibrium and $\Phi(t) \rightarrow \phi_m$, the process can be represented by a characteristic lifetime τ_d, where

$$\tau_d = (N_d C_n)^{-1} \exp(\phi_m / kT) \tag{A1}$$

and ϕ_m is proportional to N_d via Eq. (1). In this limit an entire locus of N_d and C_n (and σ_n) exists as permissible solutions for a single measured value of τ_d. This suggests the need to fit all of the available decay data such that $\Phi(t) < \phi_m$ subject to the constraint $[R_m - r_o(t_o)]$ is greater than roughly $4-5L$ in an effort to escape ambiguous solutions.

As an example, we use as input data the hypothetical case illustrated in Fig. 11(b) where $N_d = 5 \times 10^{16}$ cm^{-3} and $\sigma_n = 1 \times 10^{-21}$ cm^2 were used to compute the decay of the normalized photocurrent. We then fit these data using a least-squares routine that searches for the minimum squared deviation between the data and the solution of Eq. (4) over a span of N_d and σ_n. The result is illustrated in the respective three dimensional (3D) and shaded plan view relief maps of Figs. 17 and 18. The x and y axes are the respective scaled ranges of N_d and σ_n and the z axis is proportional to the logarithm of the sum-squared deviation. The topography of the map reveals that the expected solution ($N_d = 5 \times 10^{16}$ cm^{-3} and $\sigma_n = 1 \times 10^{-21}$ cm^2) appears as a pole, but that there is also a continuous remnant local minimum appearing as a locus satisfying Eq. (A1) for the special case under consideration (with $\tau_d = 90.12$ s for this hypothetical example). The dashed curve appearing in Fig. 18 is a separate computed solution of Eq. (A1) superimposed on the relief map to illustrate that the remnant continuous minimum revealed from the least-squares fitting procedure indeed conforms to the limiting case represented by the solution of Eq. (A1). This result also demonstrates that the efficiency of the least-squares fitting procedure can be substantially improved by restricting the search grid of N_d and σ_n to only follow a band of these parameters in the vicinity of the remnant solution.

[1] Y. Huang, X. Duan, Y. Cui, and C. M. Lieber, Nano Lett. **2**, 101 (2002).
[2] F. Qian, S. Gradečak, Y. Li, C.-Y. Wen, and C. M. Lieber, Nano Lett. **5**, 2287 (2005).
[3] M. C. McAlpine, R. S. Friedman, S. Jin, K.-h. Lin, W. U. Wang, and C. M. Lieber, Nano Lett. **3**, 1531 (2003).
[4] D. Tham, C.-Y. Nam, and J. E. Fischer, Adv. Funct. Mater. **16**, 1197

(2006).
[5]K. A. Bertness, N. A. Sanford, J. M. Barker, J. B. Schlager, A. Roshko, A. V. Davydov, and I. Levin, J. Electron. Mater. **35**, 576 (2006).
[6]K. A. Bertness, A. Roshko, L. M. Mansfield, T. E. Harvey, and N. A. Sanford, J. Cryst. Growth **300**, 94 (2007).
[7]J. B. Schlager, N. A. Sanford, K. A. Bertness, J. M. Barker, A. Roshko, and P. T. Blanchard, Appl. Phys. Lett. **88**, 213106 (2006).
[8]J. B. Schlager, K. A. Bertness, P. T. Blanchard, L. H. Robins, A. Roshko, and N. A. Sanford, J. Appl. Phys. **103**, 124309 (2008).
[9]S. M. Tanner, J. M. Gray, C. T. Rogers, K. A. Bertness, and N. A. Sanford, Appl. Phys. Lett. **91**, 203117 (2007).
[10]J. Ristić, E. Calleja, M. A. Sánchez-García, J. M. Ulloa, J. Sánchez-Páramo, J. M. Calleja, U. Jahn, A. Trampert, and K. H. Ploog, Phys. Rev. B **68**, 125305 (2003).
[11]H. Sekiguchi, K. Kato, J. Tanaka, A. Kikuchi, and K. Kishino, Phys. Status Solidi A **205**, 1067 (2008).
[12]H.-M. Kim, Y.-H. Cho, H. Lee, S. I. Kim, S. R. Ryu, D. Y. Kim, T. W. Kang, and K. S. Chung, Nano Lett. **4**, 1059 (2004).
[13]R. Calarco, M. Marso, T. Richter, A. I. Aykanat, R. Meijers, A. v.d. Hart, T. Stoica, and H. Lüth, Nano Lett. **5**, 981 (2005).
[14]V. Dobrokhotov, D. N. McIlroy, M. G. Norton, A. Abuzir, W. J. Yeh, I. Stevenson, R. Pouy, J. Bochenek, M. Cartwright, L. Wang, J. Dawson, M. Beaux, and C. Berven, J. Appl. Phys. **99**, 104302 (2006).
[15]X. Duan, Y. Huang, and C. M. Lieber, Nano Lett. **2**, 487 (2002).
[16]P. T. Blanchard, K. A. Bertness, T. E. Harvey, L. M. Mansfield, A. W. Sanders, and N. A. Sanford, IEEE Trans. Nanotechnol. **7**, 760 (2008).
[17]E. Monroy, F. Omnès, and F. Calle, Semicond. Sci. Technol. **18**, R33 (2003).
[18]A. Armstrong, G. T. Wang, and A. A. Talin, J. Electron. Mater. **38**, 484 (2009).
[19]T. Richter, H. Lüth, R. Meijers, R. Calarco, and M. Marso, Nano Lett. **8**, 3056 (2008).
[20]L. M. Mansfield, K. A. Bertness, P. T. Blanchard, T. E. Harvey, A. W. Sanders, and N. A. Sanford, J. Electron. Mater. **38**, 495 (2009).
[21]A. Motayed, M. He, A. V. Davydov, J. Melngailis, and S. N. Mohammad, J. Appl. Phys. **100**, 114310 (2006).
[22]C. J. Lu, A. V. Davydov, D. Josell, and L. A. Bendersky, J. Appl. Phys. **94**, 245 (2003).
[23]D.-F. Wang, F. Shiwei, C. Lu, A. Motayed, M. Jah, S. N. Mohammad, K. A. Jones, and L. Salamanca-Riba, J. Appl. Phys. **89**, 6214 (2001).
[24]B. P. Luther, S. E. Mohney, T. N. Jackson, M. A. Khan, Q. Chen, and J. W. Wang, Appl. Phys. Lett. **70**, 57 (1997).
[25]S. E. Mohney, Y. Wang, M. A. Cabassi, K. K. Lew, S. Dey, J. M. Redwing, and T. S. Mayer, Solid-State Electron. **49**, 227 (2005).
[26]S. Nikishin, G. Kipshidze, V. Kuryatkov, K. Choi, Ìu. Gherasoiu, L. Grave de Peralta, A. Zubrilov, V. Tretyakov, K. Copeland, T. Prokofyeva, M. Holtz, R. Asomoza, Yu. Kudryavtsev, and H. Temkin, J. Vac. Sci. Technol. B **19**, 1409 (2001).
[27]H. Morkoç, *Nitride Semiconductors and Devices* (Springer-Verlag, Berlin, 1999).
[28]R. K. Ahrenkiel, *Semiconductors and Semimetals* (Academic, New York, 1993), Vol. 39, Chap. 2.
[29]J. F. Muth, J. D. Brown, M. A. L. Johnson, Z. Yu, R. M. Kolbas, J. W. Cook, Jr., and J. F. Schentzina, MRS Internet J. Nitride Semicond. Res. **4S1**, G5.2 (1999).
[30]M. Shur, *Physics of Semiconductor Devices* (Prentice-Hall, Inc., Upper Saddle River, NJ, 1990).
[31]M. Kočan, A. Rizzi, H. Lüth, S. Keller, and U. K. Mishra, Phys. Status Solidi B **234**, 773 (2002).
[32]R. S. Muller and T. I. Kamins, *Device Electronics for Integrated Circuits*, 3rd ed. (Wiley, New York, 2003).
[33]S. Chevtchenko, X. Ni, Q. Fan, A. A. Baski, and H. Morkoç, Appl. Phys. Lett. **88**, 122104 (2006).
[34]D. Segev and C. G. Van de Walle, Europhys. Lett. **76**, 305 (2006).
[35]Simulation performed by Benjamin Klein, Georgia Institute of Technology, Savannah, GA.
[36]A. Many, Y. Goldstein, and N. B. Grover, *Semiconductor Surfaces* (North-Holland, Amsterdam, 1965), p. 138, Eq. (4.12).
[37]M. A. Reshchikov, S. Sabuktagin, D. K. Johnstone, and H. Morkoç, J. Appl. Phys. **96**, 2556 (2004).
[38]B. Carnahan, H. A. Luther, and J. O. Wilkes, *Applied Numerical Methods* (Wiley, New York, 1969), p. 363, Eq. (6.66).
[39]J. A. Champion, Proc. Phys. Soc. London **79**, 662 (1962).
[40]M. T. Hirsch, J. A. Wolk, W. Walukiewicz, and E. E. Haller, Appl. Phys. Lett. **71**, 1098 (1997).
[41]A. W. Ott, J. W. Klaus, J. M. Johnson, and S. M. George, Thin Solid Films **292**, 135 (1997).
[42]J. W. Elam, M. D. Groner, and S. M. George, Rev. Sci. Instrum. **73**, 2981 (2002).
[43]M. D. Groner, F. H. Fabreguette, J. W. Elam, and S. M. George, Chem. Mater. **16**, 639 (2004).
[44]Y. Q. Wu, T. Shen, P. D. Ye, and G. D. Wilk, Appl. Phys. Lett. **90**, 143504 (2007).
[45]M. Kang, J.-S. Lee, S.-K. Sim, H. Kim, B. Min, K. Cho, G.-T. Kim, M.-Y. Sung, S. Kim, and H. S. Han, Jpn. J. Appl. Phys. **43**, 6868 (2004).
[46]B. B. Burton, A. R. Lavoie, and S. M. George, J. Electrochem. Soc. **155**, D508 (2008).
[47]H.-Y. Cha, H. Wu, Mvs. Chandrashekhar, Y. C. Choi, S. Chae, G. Koley, and M. G. Spencer, Nanotechnology **17**, 1264 (2006).
[48]D. R. Khanal and J. Wu, Nano Lett. **7**, 2778 (2007).
[49]B. Klein (private communication).
[50]M. A. Reshchikov and H. Morkoç, J. Appl. Phys. **97**, 061301 (2005).
[51]S. Han, W. Jin, D. Zhang, T. Tang, C. Li, X. Liu, Z. Liu, B. Lei, and C. Zhou, Chem. Phys. Lett. **389**, 176 (2004).